Two-dimensional phase-space picture of the photonic crystal Fano laser

Piotr M. Kamiński [1,*] Samel Arslanagić [1,†] Jesper Mørk [2] and Jensen Li [3,‡]

[1]*Department of Electrical Engineering, Technical University of Denmark, Ørsteds Plads, 2800 Kongens Lyngby, Denmark*
[2]*Department of Photonics Engineering, Technical University of Denmark, Ørsteds Plads, 2800 Kongens Lyngby, Denmark*
[3]*Department of Physics, Hong Kong University of Science and Technology, Clear Water Bay, Hong Kong, China*

(Received 3 March 2019; published 6 November 2019)

The recently realized photonic-crystal Fano laser constitutes the first demonstration of passive pulse generation in nanolasers [Yi Yu *et al.*, Nat. Photon. **11**, 81 (2017)]. We show that the laser operation is confined to only two degrees of freedom after the initial transition stage. We show that the original five-dimensional dynamic model can be reduced to a one-dimensional model in a narrow region of the parameter space and it evolves into a two-dimensional (2D) model after the exceptional point, where the eigenvalues transition from being purely real to a complex conjugate pair. The 2D reduced model allows us to establish an effective band structure for the eigenvalue problem of the stability matrix and to explain the laser dynamics. The reduced model is used to associate an origin of instability with an unstable periodic orbit separating the stable steady state from the stable periodic orbit.

DOI: 10.1103/PhysRevA.100.053808

I. INTRODUCTION

Integrated photonic circuits require energy-efficient, fast, and compact light sources [1]. Particularly promising candidates to realize them are photonic-crystal (PC) lasers due to their flexibility in design and precise control of the cavity properties [2,3]. PC lasers can be electrically driven and allow for modulation in the GHz range [4,5]. Moreover, they have been shown to exhibit very rich dynamics, e.g., spontaneous symmetry breaking [6]. Recently, a new type of PC laser has been proposed [7] where one of the mirrors arises due to a Fano resonance [8,9]. Furthermore, this laser has been demonstrated to be able to generate a self-sustained train of pulses at GHz frequencies, a property that has been observed only in macroscopic lasers thus far [10]. The generation of pulses by an ultracompact laser is of interest for applications in future on-chip optical signal processing.

The configuration of the Fano laser is shown in Fig. 1. The active material may be composed of several layers of InAs quantum dots or quantum wells and is incorporated inside the InP PC membrane. The laser cavity is composed of a PC line-defect waveguide blocked with a PC mirror on the left side, forming a broadband mirror, whereas the right mirror is due to the Fano interference between the nanocavity and the waveguide. The Fano resonance arises due to the interference of a discrete mode of the nanocavity with the continuum of PC waveguide modes. The spectral width of the resonance is determined by the quality factor of the nanocavity enabling the realization of a narrowband mirror. The dynamic operation of the laser is modeled using a combination of coupled-mode theory and conventional laser rate equations [11]. The model has been used to demonstrate that there are two regimes of operation: the continuous-wave regime and a self-pulsing regime [11]. Particularly, it has been shown that as the real part of any of the eigenvalues of the underlying stability matrix, evaluated at the steady state, becomes positive, the relaxation oscillation becomes undamped, resulting in the laser becoming unstable and self-pulsing behavior setting in [11,12]. However, it does not fully explain the origin of instability in the whole parameter space of the laser as there exists a region in which the laser can become unstable even when all the steady-state eigenvalues are negative [11].

The purpose of this work is to analyze not only the steady-state eigenvalues of the stability matrix of the dynamic model, but also the instantaneous eigenvalues during the laser operation. Moreover, we determine the "minimal" model for the laser that is required to explain the dynamics in different regimes, thereby obtaining an alternative perspective on the dynamics of the Fano laser. We thus demonstrate that the laser operation can be effectively modeled by a one-dimensional (1D) system of differential equations in a limited region of the parameter space when the steady-state eigenvalues are purely real and that it evolves into an effective two-dimensional (2D) system beyond the steady-state exceptional point, when the eigenvalues form complex conjugate pairs. These findings are used to determine the origin of the instability that is observed when the steady-state eigenvalues are negative. We notice that the analysis of instabilities and chaos in injection-locked lasers, e.g., using bifurcation analysis, has been very successful [13–16]. Here, we use it to analyze the origin of laser instability when the steady state is stable and set an important goal to identify reduced systems for getting further physical insight.

The paper is organized as follows. In Sec. II, we introduce the model used to describe the laser dynamics. In Sec. III, we show that the laser operation can be understood by means of a 2D phase-space picture and we analyze the steady state and

*pmarka@elektro.dtu.dk
†sar@elektro.dtu.dk
‡jensenli@ust.hk

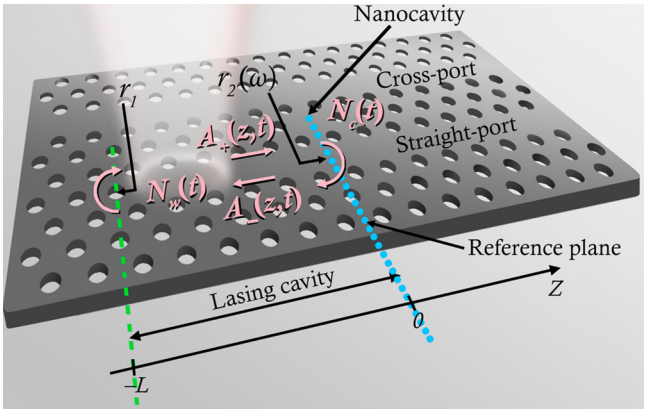

FIG. 1. Schematic of a PC Fano laser. The active material is uniformly incorporated in the PC slab. The lasing cavity is composed of a PC line-defect waveguide terminated with a broadband mirror (the dashed green line) and a narrowband mirror due to the Fano interference between the nanocavity and the waveguide. The length of the lasing cavity is defined as the distance between the broadband mirror and a reference plane (the dotted blue line). The dynamic variables are marked in pink and are the carrier densities in the waveguide and the nanocavity, $N_w(t)$ and $N_c(t)$, respectively, and the right- and left-propagating complex field envelopes, $A_+(0,t)$ and $A_-(0,t)$, respectively, evaluated at the reference plane.

instantaneous eigenvalues of the stability matrix. In Sec. IV, we exploit the simplified 2D model to associate a self-pulsing operation, when a steady state is stable to a generalized Hopf (Bautin) bifurcation, which is characterized by a bifurcation of two periodic orbits and an equilibrium point (steady state) [17,18].

II. DYNAMIC MODEL OF THE FANO LASER

We next briefly describe the procedure required to establish the dynamic model of the Fano laser; for more details, refer to [11]. The complex field is decomposed into the fields propagating to the right and left from the reference plane; see Fig. 1. By combining the boundary conditions for both fields, we can arrive at the oscillation condition [7]:

$$r_1(\omega_s)r_R(\omega_s,\omega_c)e^{i2k(\omega_s,N_s)L}=1, \tag{1}$$

where r_1 and r_R are the broadband (left) and the narrowband (right) reflection coefficients, respectively. r_R is determined using the coupled-mode theory [19–21], while r_1 is the reflection coefficient due to the PC band gap and has to be transformed towards the common reference plane using standard transmission-line theory [22]. k is the complex wave number of the waveguide, L is the length of the lasing cavity, and ω_c is the resonance frequency of the nanocavity. The condition in Eq. (1) is solved for (ω_s, N_s), which are the steady-state lasing frequency and carrier density, respectively. They serve as expansion points of the dynamic model. There are multiple solutions of Eq. (1) [7,12], from among which the one with the lowest modal threshold gain is chosen. The wave number k accounts for dispersion of the refractive index of the PC membrane and the gain of the active material.

Subsequently, the boundary condition is solved for the left-propagating field and then the term $1/(r_1(\omega)e^{i2k(\omega_s,N_s)L})$ is Taylor expanded around the steady-state operation point (ω_s, N_s) and a first-order differential equation for the right-propagating complex field envelope evaluated at the reference plane $A_+(t)$ is derived using the Fourier transform. In the special case of an open waveguide considered here, the coupled-mode equation for the field in the nanocavity can be directly reformulated as an equation for the left-propagating complex field envelope evaluated at the reference plane $A_-(t)$. The equations for $A_+(t)$ and $A_-(t)$ are complemented with the traditional rate equations for carrier densities in the waveguide and the nanocavity.

Since the variables introduced above differ by orders of magnitude, we introduce dimensionless near-unity variables in order to improve numerical stability. Moreover, detuning from the expansion point frequency ω_s results in time-varying real and imaginary parts of $A_+(t)$ and $A_-(t)$ at the steady state. Because of that, the differential equations for $A_+(t)$ and $A_-(t)$ are separated into equations for amplitudes and phase evolutions by the following substitution: $A_+(t)=A_{0+}|a_+(\tau/(G_{NC}N_0))|e^{i\phi_+(\tau/(G_{NC}N_0))}$, $A_-(t)=A_{0-}|a_-(\tau/(G_{NC}N_0))|e^{i\phi_-(\tau/(G_{NC}N_0))}$, where A_{0+} and A_{0-} are the normalization constants, $a_-(\tau)$ and $a_+(\tau)$ are the normalized complex field envelopes, $\tau=tG_{NC}N_0$ is the normalized time, $G_{NC}=\Gamma_C v_g g_N$, and v_g is the group velocity. The system depends solely on the phase difference $\Delta\phi(\tau)=\phi_-(\tau)-\phi_+(\tau)$; thus, by subtracting the equations for phase evolutions $\phi_+(\tau)$, $\phi_-(\tau)$ and exploiting the linearity of differentiation, these equations can be combined into one. This leads us to the following system of five differential equations describing the dynamics of the laser:

$$\frac{d|a_+(\tau)|}{d\tau}=-\frac{\gamma_L|a_+(\tau)|}{G_{NC}N_0}+\frac{\Gamma|a_+(\tau)|(n_w(\tau)-n_s)}{2\Gamma_C}+\frac{\gamma_L}{G_{NC}N_0}|a_+(\tau)|\mathrm{Re}\left(\frac{A_-(\tau)}{r_RA_+(\tau)}\right), \tag{2a}$$

$$\frac{d|a_-(\tau)|}{d\tau}=-\frac{P\gamma_C}{G_{NC}N_0}|a_-(\tau)|\mathrm{Re}\left(\frac{A_+(\tau)}{A_-(\tau)}\right)-\frac{\gamma_T|a_-(\tau)|}{G_{NC}N_0}+\frac{|a_-(\tau)|(n_c(\tau)-1)}{2}, \tag{2b}$$

$$\frac{d\Delta\phi(\tau)}{d\tau}=-\frac{\alpha}{2}(n_c(\tau)-1)+\frac{\Gamma\alpha(n_w(\tau)-n_s)}{2\Gamma_C}-\frac{\Delta\omega}{G_{NC}N_0}-\mathrm{Im}\left(\frac{r_RP\gamma_CA_+^2(\tau)+\gamma_LA_-^2(\tau)}{r_RG_{NC}N_0A_-(\tau)A_+(\tau)}\right), \tag{2c}$$

$$\frac{dn_w(\tau)}{d\tau}=\frac{-|a_+(\tau)|^2(n_w(\tau)-1)-n_w(\tau)+j_c}{G_{NC}N_0\tau_s}, \tag{2d}$$

$$\frac{dn_c(\tau)}{d\tau}=\frac{-|a_-(\tau)|^2(n_c(\tau)-1)-n_c(\tau)}{G_{NC}N_0\tau_c}. \tag{2e}$$

Here, $n_w(\tau)$ and $n_c(\tau)$ are the carrier densities in the waveguide and the nanocavity, respectively, normalized with respect to the transparency carrier density N_0. $\gamma_L=v_g/(2L)$ is the inverse of the cavity round-trip time, n_s is the steady-state carrier density obtained from the oscillation condition normalized with respect to N_0, $\Delta\omega=\omega_c-\omega_s$ is the detuning of the steady-state lasing frequency ω_s from the cavity resonance frequency ω_c, and j_c is the normalized effective pumping current, which includes the injection efficiency.

Subsequently, we linearize the problem by calculating the total derivative of Eqs. (2) with respect to τ. The system of equations describing the laser dynamics in Eqs. (2) can be expressed in the short form as a function $V(\cdot)$ of the state vector $\vec{\psi}(\tau)$:

$$\vec{\psi}(\tau) = \{|a_+(\tau)|, |a_-(\tau)|, \Delta\phi(\tau), n_w(\tau), n_c(\tau)\}, \quad (3a)$$

$$\frac{d\vec{\psi}(\tau)}{d\tau} = V(\vec{\psi}(\tau)). \quad (3b)$$

By taking the total derivative of $V(\vec{\psi}(\tau))$, we obtain a directional derivative along the curve parameterized by τ:

$$\frac{d^2\vec{\psi}(\tau)}{d\tau^2} = \nabla_{\vec{\psi}} V(\vec{\psi}(\tau)) \frac{d\vec{\psi}(\tau)}{d\tau} = \boldsymbol{A}(\vec{\psi}(\tau)) \frac{d\vec{\psi}(\tau)}{d\tau}. \quad (4)$$

Consequently, $d\vec{\psi}(\tau)/d\tau$ in Eq. (3b) is interpreted as the velocity of the state vector and is expressed as a function of the current position of the state vector in Eq. (2). $d^2\vec{\psi}(\tau)/d\tau^2$ is interpreted as the acceleration of the state vector; see Eq. (4). Matrix $\boldsymbol{A}$ is the so-called Jacobian matrix; its eigenvalues λ are used to determine the stability of the laser when evaluated at the steady state. The system is stable if all eigenvalues have negative real parts. On the other hand, if any eigenvalue has a positive real part, the system is unstable. The matrix $\boldsymbol{A}$ is purely real, but not symmetric as we separated the complex field envelopes into the magnitudes $|a_+(\tau)|$, $|a_-(\tau)|$ and the phase difference $\Delta\phi$. Therefore, the matrix is non-Hermitian and we have to distinguish between right $\vec{v}$ and left $\vec{w}$ eigenvectors, which are normalized so that $\boldsymbol{W}^T\boldsymbol{V} = \boldsymbol{I}$ is satisfied [23,24]. The columns of $\boldsymbol{W}$ and $\boldsymbol{V}$ are the left and the right eigenvectors, and $\boldsymbol{I}$ is the identity matrix. Furthermore, eigenvalues of the matrix $\boldsymbol{A}$ can be purely real or form complex conjugate pairs [25]. In the following sections, we use Eqs. (2) and (3) to investigate the origin of instability in the case of a stable steady state and to show that the original laser model can be simplified to a system of two differential equations.

III. TWO-DIMENSIONAL PHASE-SPACE PICTURE

A. Steady-state eigenvalues

Above the threshold, the laser can exhibit two types of operation: the continuous wave and the self-pulsing operation [10,11]. Figure 2 shows the real and imaginary parts of the two steady-state eigenvalues of the Jacobian matrix $\boldsymbol{A}$, with the largest real parts plotted versus $\Delta\omega_c$, which is the detuning of the cavity resonance frequency ω_c from the resonance frequency of the isolated cavity, normalized with respect to γ_T. It is noted that $\Delta\omega_c$ defines $\Delta\omega$ in Eq. (2) through the oscillation condition, given by Eq. (1), and is controlled externally. As our case study, we choose $\Delta\omega_c$ marked with the blue line in Fig. 2.

Interestingly, it has been observed in [11] that in the vicinity of the $\Delta\omega_c$ marked by the blue dashed line in Fig. 2, the laser can exhibit the continuous wave or the self-pulsing operation depending on the initial condition despite its steady-state eigenvalues having negative real parts, and thus suggesting stable operation of the laser. However, the origin of this instability has not been explained and is examined in Sec. IV. On the other hand, when $\Delta\omega_c$ is increased beyond $1.26\gamma_T$, the real parts become positive, the relaxation oscillation becomes undamped, the laser becomes unstable, and the state approaches a stable periodic orbit for any initial condition [11]. All of the following figures are obtained for the parameters listed in Table I, while the pumping current is set to $J = 1.2J_{\text{thr}}$, where J_{thr} is the minimum threshold current.

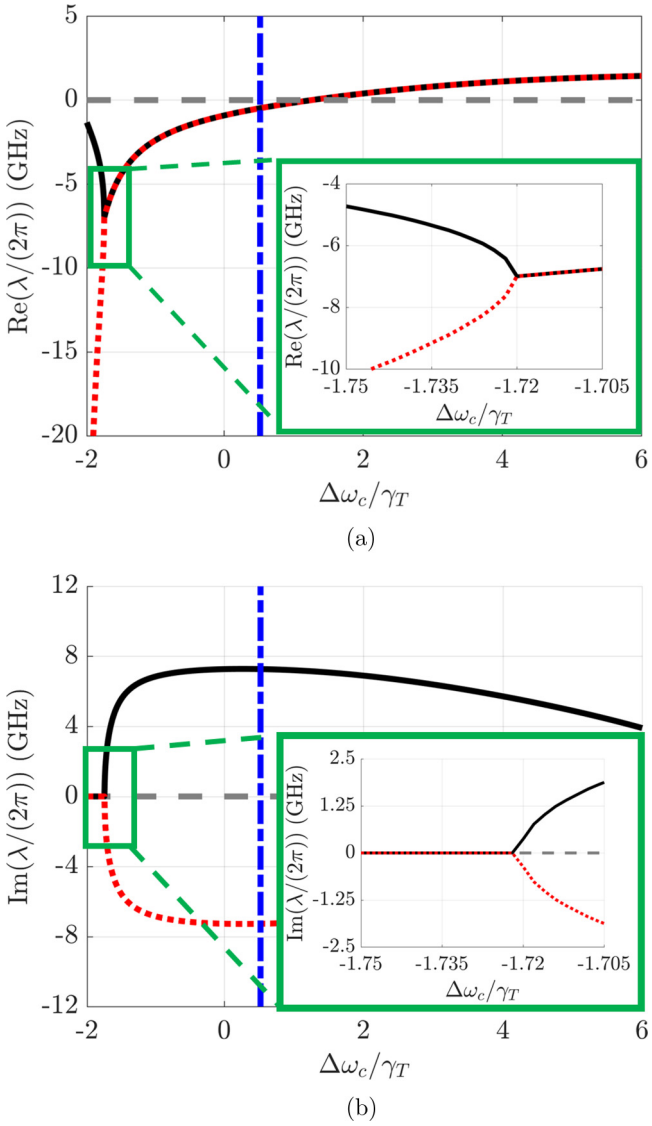

FIG. 2. (a) Real and (b) imaginary parts of the two steady-state eigenvalues of the matrix $\boldsymbol{A}$ with the largest real parts. The horizontal dashed gray line indicates zero. The vertical dot-dashed blue line indicates $\Delta\omega_c$ for which Fig. 3 is obtained. The pumping current is set to $J = 1.2J_{\text{thr}}$. The green frame marks the position of the exceptional point, while the insets show the eigenvalues in its vicinity.

B. Exceptional points

It is interesting to observe in Fig. 2 that for $\Delta\omega_c$ lower than $-1.72\gamma_T$, the real part of the two eigenvalues splits and the eigenvalues become purely real; see Fig. 2(b). At $\Delta\omega_c = -1.72\gamma_T$, the two eigenvalues coalesce and not only

TABLE I. Laser parameters used in all numerical simulations.

Parameter name	Symbol	Value
Transparency carrier density	N_0	1×10^{24} m^{-3}
Parity of the cavity mode	P	1
Linewidth enhancement factor	α	1
Internal loss factor	α_i	1000 m^{-1}
Lasing cavity length	L	5 μm
Carrier lifetimes	τ_s, τ_c	0.5 ns
Laser cavity volume	V_{LC}	1.05 μm^3
Nanocavity volume	V_{NC}	0.243 μm^3
Nanocavity resonance	λ_r	1554 nm
Reference refractive index	n_{ref}	3.5
Group refractive index	n_{grp}	3.5
Differential gain	g_N	5×10^{-20} m^2
Waveguide confinement factor	Γ	0.5
Nanocavity confinement factor	Γ_C	0.3
Left mirror reflectivity	R_1	1
Nanocavity-waveguide coupling	γ_C	1.14 ps^{-1}
Nanocavity total passive decay rate	γ_T	1.21 ps^{-1}

are the eigenvalues identical at this point, but so are the eigenvectors [26–30]. This constitutes an exceptional point which is also known as a symmetry-breaking point for a non-Hermitian system [31–34]. However, exceptional points are a general phenomenon observed in optical waveguides [35], unstable laser resonators [36], coupled PC nanolasers [37], quantum systems [38], electronic circuits [39], and mechanical resonators [40]. They only require non-Hermiticity of the system for their existence [27,28,41]. We emphasize that exceptional points may arise upon coalescence of eigenvectors and eigenvalues of any matrix, e.g., a Hamiltonian matrix [42], an S-parameter matrix [43], and impedance or admittance matrices [44], to name a few. Exceptional points have also been linked to a self-pulsing mechanism in distributed feedback lasers [45,46], in which case the self-pulsing mechanism was attributed to the dispersive quality factor self-switching similarly as in the case of the Fano laser [10]. In the present case, exceptional points arise due to dissimilar decay rates, γ_C, γ_L and phenomenologically introduced gain terms $|a(\tau)|(n(\tau) - 1)$; see Eqs. (2) and (2b). They play an analogous role to the loss and gain usually introduced as an imaginary part of the refractive index in parity-time symmetric systems [47,48].

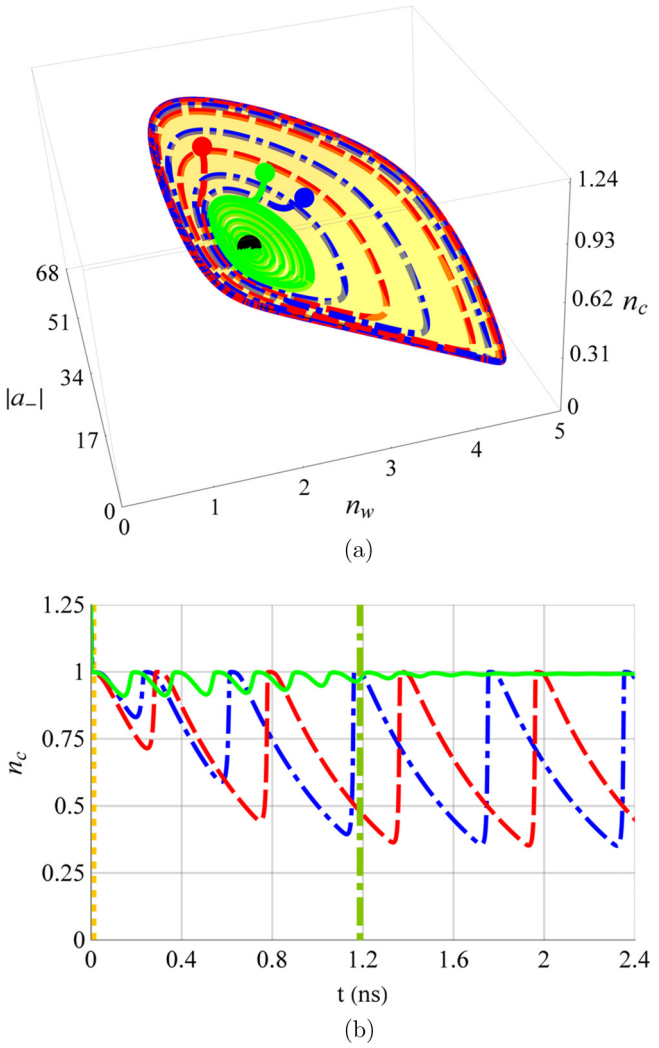

FIG. 3. (a) The trajectories of n_c against n_w and $|a_-|$. The black dot on the yellow surface represents the steady state. The red, green, and blue dots above the yellow surface are the three different initial conditions. During an initial transition stage, the state decays towards the surface. Then the state continues its evolution on the surface. (b) The trajectories in time domain show the initial transition stage lasting a few ps, the later transition stage lasting ∼1.2 ns, and, finally, the self-pulsing stage at the edge of the surface. The vertical orange dotted and green dash-dotted lines mark the end of the initial and later transition stage, respectively.

C. Two-dimensional phase space

In Fig. 3, we plot three trajectories of n_c, marked in red, green, and blue, versus n_w, $|a_-|$ and obtained for the three different initial conditions. The trajectories are parameterized by τ. It is found that there are actually three different stages of the laser operation: the initial transition stage, the later transition stage, and the self-pulsing stage. This is in contrast to the previously reported picture of two stages: the transition stage and the self-pulsing stage. The red, green, and blue dots mark the initial conditions in Fig. 3. It is found that at first, they lie above a yellow surface; this is the initial transition stage which lasts only a few picoseconds. After a very short initial transition stage, the state reaches the surface at the time instant marked with the orange dotted line in Fig. 3(b). The state stays on the surface within the later transition and the self-pulsing or continuous-wave stage. Eventually, the state reaches the stable periodic orbit at the time instant marked with the green dash-dotted line in Fig. 3(b). The state stays at the orbit unless perturbed; this stage is called the self-pulsing stage and takes place at the edge of the yellow surface.

Thus, it is found that once the state reaches the yellow surface, the state is confined to the surface. The phenomenon of data collapse to a surface also happens for the other two variables, $|a_+|$, $\Delta\phi$. Since the state always lies on the surface after a very short initial time, we conclude that two degrees of freedom are sufficient to specify the state after

the initial transition stage and the propagation of the state is locally restricted to two directions. We note that this phenomenon is a general feature of a dynamical system close to a Hopf bifurcation and is called a reduction to the center manifold [18,49,50]. The dimension of the center manifold is strictly related to the number of steady-state eigenvalues, the real parts of which cross zero [18,49,50]. In Fig. 2(a), we have seen that in the present case, there are two eigenvalues with real parts crossing zero, while all the remaining eigenvalues have negative real parts, giving rise to a stable manifold. Thus, the center manifold is two dimensional, as confirmed by the yellow curved surface in Fig. 3(a). The dynamics in the remaining three directions quickly approach the surface during the initial transition stage.

In Fig. 3, n_w and $|a_-|$ are the two degrees of freedom, while all the remaining degrees of freedom $\{|a_+|, \Delta\phi, n_c\}$ of the state vector $\vec{\psi}$ are expressed as functions of the variables n_w and $|a_-|$ after the initial transition stage:

$$\vec{\psi} = \{|a_+(|a_-|, n_w)|, |a_-|, \Delta\phi(|a_-|, n_w), n_w, n_c(|a_-|, n_w)\}. \tag{5a}$$

Similarly, equations for each component of the velocity vector $d\vec{\psi}/d\tau$ in Eqs. (2) and (3b) can be expressed as functions of n_w and $|a_-|$:

$$\frac{d\vec{\psi}}{d\tau} = \{V_1(|a_-|, n_w), V_2(|a_-|, n_w), V_3(|a_-|, n_w), \times V_4(|a_-|, n_w), V_5(|a_-|, n_w)\}. \tag{5b}$$

By taking the total derivative of $d\vec{\psi}(\tau)/d\tau$, we obtain

$$\left[\frac{d^2\vec{\psi}(\tau)}{d\tau^2}\right]_i = \left\{\frac{\partial V_i}{\partial |a_-|}\frac{d|a_-|}{d\tau} + \frac{\partial V_i}{\partial n_w}\frac{dn_w}{d\tau}\right\}, \tag{6}$$

which, when compared with Eq. (4), indicates that the laser dynamics can be locally approximated by a 2×2 Jacobian matrix $\boldsymbol{A}$.

The functions of n_w and $|a_-|$ in Eq. (5a) and the yellow surface in Fig. 3 are approximated by polynomials. In order to do that, we solve the system of differential equations in Eqs. (2) for varying initial conditions. Each solution then corresponds to a different trajectory plotted versus n_w and $|a_-|$. All of these trajectories are seen to lie on the surface after the initial transition stage similarly to Fig. 3. Next, we fit a polynomial with all the trajectories excluding the initial transition stage. Then the polynomial describes the surface n_c in terms of n_w and $|a_-|$. Similarly, we can approximate the surfaces for $|a_+(|a_-|, n_w)|$ and $\Delta\phi(|a_-|, n_w)$. We emphasize that in order to keep the original coordinate system of the variables, we exclude the part of the trajectory in the initial transition stage and fit a polynomial with the remaining parts of all the trajectories. Thus, we fit the polynomials once the state has reached the center manifold. Having obtained these surfaces, we can determine any state in the phase space within the periodic orbit once n_w and $|a_-|$ are known without any need of solving the five-dimensional system of equations in Eq. (2).

Moreover, in order to describe the dynamics on these surfaces, we need to solve a system of two differential equations describing the two degrees of freedom, n_w and $|a_-|$. These equations are the components of the velocity vector in Eq. (5b),

$$\frac{d|a_-(\tau)|}{d\tau} = V_2(|a_-(\tau)|, n_w(\tau)), \tag{7a}$$

$$\frac{dn_w(\tau)}{d\tau} = V_4(|a_-(\tau)|, n_w(\tau)). \tag{7b}$$

Once Eq. (7) is solved, the remaining degrees of freedom $\{|a_+|, \Delta\phi, n_c\}$ can be determined using the polynomials.

D. Instantaneous eigenvalues

We compute the instantaneous eigenvalues of the matrix $\boldsymbol{A}$ in Eq. (4) for the state vectors $\vec{\psi}$, given by Eq. (5a), over the whole surfaces. In Fig. 3, we have seen that we can define three surfaces for $|a_+|$, $\Delta\phi$, n_c plotted versus n_w and $|a_-|$. After the initial transition stage, the state always lies on these surfaces. Thus, all the dynamics are confined to these surfaces. Then, each point of these surfaces can be substituted into the matrix $\boldsymbol{A}$ and the instantaneous eigenvalues of the state at this position are obtained. Figure 4 shows the real and imaginary parts of the three instantaneous eigenvalues, with the largest real parts over the whole surface as well as along the trajectory marked with the green dashed line. The two remaining eigenvalues have significantly smaller real parts, and thus are not included in Fig. 4 as the contribution from the corresponding eigenvectors decays rapidly.

Figure 4(a) shows that the pair of eigenvalues marked with orange and yellow has considerably larger real parts than the third eigenvalue (purple) over the major part of the surface. The third eigenvalue is only comparable to the other two eigenvalues along the line $|a_-| = 0$, but it is still smaller and never becomes positive. The negative real parts of the purely real third eigenvalue (purple) and the remaining complex conjugate pair of eigenvalues (not shown) signify that the contribution of the corresponding eigenvectors in a reconstruction of the solution decays very quickly. This is what is observed in Fig. 3 in the initial transition stage. Afterwards, once the state is on the surface, the contribution from the three corresponding eigenvectors is negligible and the state description is dominated by the eigenvectors corresponding to the two eigenvalues with the largest real part (orange and yellow).

The real parts of the pair of eigenvalues marked with orange and yellow are seen to dominate for large values of $|a_-|$; this is where the pulse is released. In Figs. 4(c)–4(e), we show the instantaneous eigenvalues in the vicinity of the pulse along the green trajectory in Figs. 4(a) and 4(b) when the state has already reached a limit cycle. On the right axis, we plot the pulse power in the straight port defined as

$$P_+(t) = 2\epsilon_0 n_{ref} c_0 |A_+(t) + PA_-(t)|^2, \tag{8}$$

where c_0 is the speed of light and ϵ_0 is vacuum permittivity.

Figure 4 shows that when the state moves along the n_w axis (just after the previous pulse has been released and before a new one), the three eigenvalues with the largest real parts are purely real. As the limiting value of n_w is reached [Fig. 4(a)], one of the eigenvalues (orange) starts to rapidly increase [Fig. 4(c)], while the third eigenvalue (purple) drops rapidly. Just as the pulse is released, the second eigenvalue

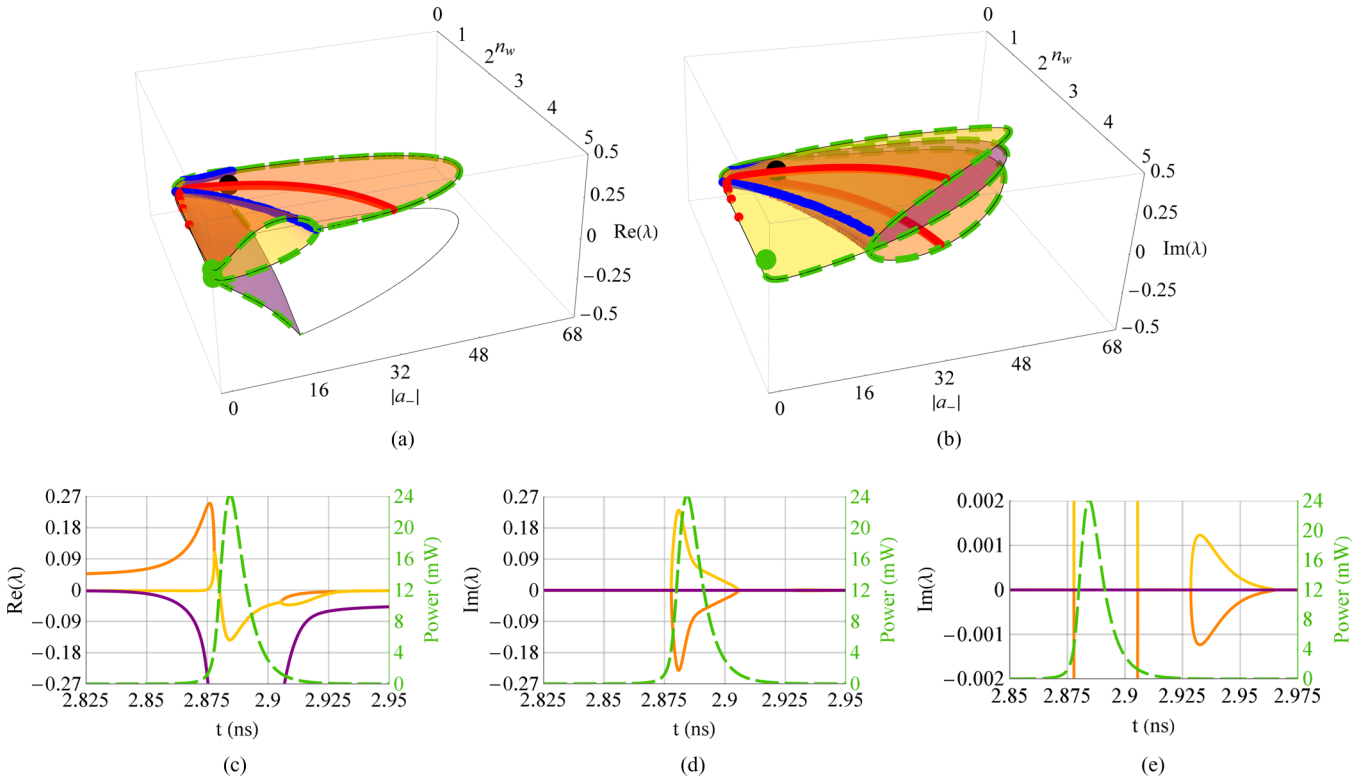

FIG. 4. (a) Real and (b) imaginary parts of the three instantaneous eigenvalues, λ, of $\boldsymbol{A}$ with the largest real parts. The eigenvalues form a complex conjugate pair marked with orange and yellow (light gray); the remaining eigenvalue is purely real and marked with purple (dark gray). The red (gray) line indicates the positions when $\mathrm{Re}(\lambda) = 0$. The blue (very dark gray) line indicates the contours of exceptional points. The black dot indicates the eigenvalues at the steady state. The green dot at the edge of the surface indicates initial eigenvalues of the trajectory, marked with the dashed green line, plotted in (c) and (d). (c) Real and (d) imaginary parts of the instantaneous eigenvalues, with the largest real parts along the green trajectory in (a) and (b). The pulse power in the straight port is marked with a dashed green line (on the right axes). (e) The imaginary parts of the eigenvalues in the vicinity of the second pair of the exceptional points.

(yellow) rapidly increases and collapses with the first one (orange) at the exceptional point. Therefore, it is found that as the pulse grows, the pair of eigenvalues transitions from being purely real to being complex conjugate when crossing the exceptional point. As the pulse power decreases, the complex conjugate pair of eigenvalues coalesces at the second exceptional point and transitions back to the pair of purely real eigenvalues. Thus, most of the pulse is observed to be bounded by the two instantaneous exceptional points with the positive and negative real part of the eigenvalue at the beginning and end of the pulse, respectively. Interestingly, two more exceptional points are observed as the pulse is decaying; see Fig. 4(e).

Within one period, the state traverses a loop in the phase space of the model. We have seen that four exceptional points are crossed within a single loop when the laser state is a periodic orbit. When the exceptional point is approached, the eigenvectors exhibit a characteristic phase jump and are phase shifted relative to each other by $\pm i$ [41,51]. Therefore, during an evolution along any trajectory in the diminishing vicinity of an exceptional point, eigenvectors will acquire a phase shift of $\pm i$ [42,52,53]. In [54], it has been shown that this effect is preserved as long as the exceptional point is inside the loop or crossed by it. Therefore, it is only a fourfold loop around an exceptional point or a single loop around four exceptional points that will restore an original scenario for the eigenvectors concerned [26,27,29,55,56]. Since the laser is operating in the periodic orbit in our case, in order to remain periodic it has to cross four exceptional points within one period in phase space.

E. Reconstruction of the solution

At most two out of five instantaneous eigenvalues have positive real parts. Thus, after the initial transition stage, the eigenvectors which correspond to the two dominating eigenvalues can be used to reconstruct the solution of Eq. (4) as follows:

$$\frac{d\vec{\psi}}{d\tau} = c_1(\tau)\vec{v}_1(\tau) + c_2(\tau)\vec{v}_2(\tau), \tag{9}$$

where $\vec{v}_{1,2}$ are the instantaneous right eigenvectors and $c_{1,2}$ are the amplitudes of the corresponding eigenvectors. These amplitudes can be reconstructed from a solution $d\vec{\psi}(\tau)/d\tau$ using the left eigenvectors as $c_{1,2} = \vec{w}^T_{1,2}(\tau)d\vec{\psi}(\tau)/d\tau$. In the following, we show that the two eigenvectors can be used to approximate the two tangential vectors to the surface pointing along the $|a_-|$, n_w coordinate lines. This confirms that the solution can be approximately expanded in the two eigenvectors.

The tangential vector to the surface $z = f(x, y)$ along the parametric curve $\vec{r}(t) = \{x(t), y(t), z(t)\}$ on this surface is

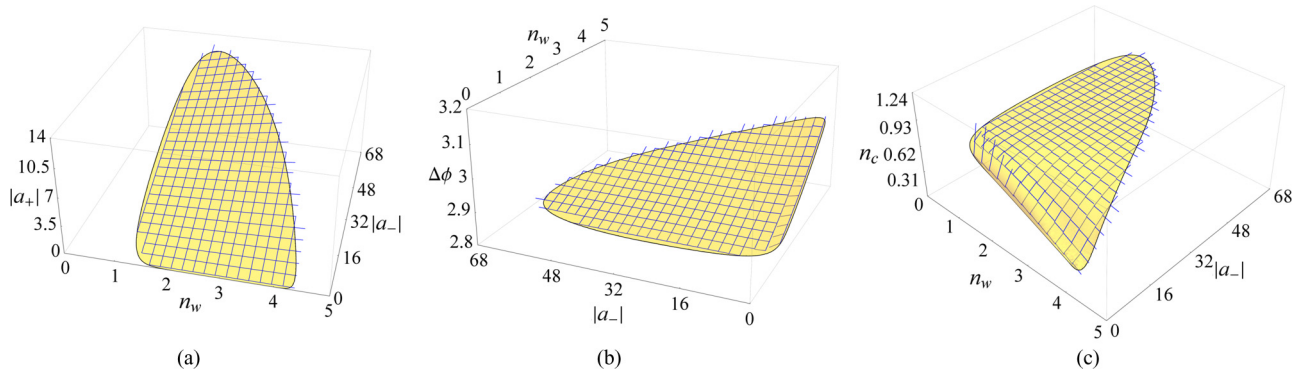

FIG. 5. The vectors $\vec{v}'_{1,2}$ plotted on the three surfaces: (a) $|a_+|$, (b) $\Delta\phi$, and (c) n_c. The vectors $\vec{v}'_{1,2}$ result from the linear combination of the eigenvectors corresponding to the top two eigenvalues and enforcing them to point along the n_w, $|a_-|$ coordinate lines. These vectors are found to approximate the tangential vectors to the surface along the n_w, $|a_-|$ coordinate lines.

expressed as $\vec{r}'(t) = \{x'(t), y'(t), z'(t)\}$, where $z'(t) = \nabla f \cdot \vec{u}$, $\vec{u} = \{x'(t), y'(t)\}$. In our case, the tangential vectors to the surfaces, which approximate the components of the state vector $\vec{\psi}$, given by Eq. (5a), are expressed as

$$\vec{r}'(\tau) = \left\{ \frac{d|a_-|}{d\tau}, \frac{dn_w}{d\tau}, \frac{d\vec{\psi}}{d\tau} \right\}, \tag{10}$$

where

$$\frac{d\vec{\psi}}{d\tau} = \frac{\partial\vec{\psi}}{\partial|a_-|}\frac{d|a_-|}{d\tau} + \frac{\partial\vec{\psi}}{\partial n_w}\frac{dn_w}{d\tau}. \tag{11}$$

The tangential vectors $\vec{r}'(\tau)$ along the parameterized trajectory can be decomposed into a linear combination of the tangential vectors to the surface along its coordinates $|a_-|, n_w$:

$$\vec{r}'_1 = \left\{1, 0, \frac{\partial\vec{\psi}}{\partial|a_-|}\right\}, \qquad \vec{r}'_2 = \left\{0, 1, \frac{\partial\vec{\psi}}{\partial n_w}\right\}. \tag{12}$$

It is observed that the tangential vectors to the surface are composed of the components of the velocity vector, given by Eq. (10), and the velocity vector can be expanded into the two eigenvectors; see Eq. (9). Since the five-dimensional (5D) matrix $\boldsymbol{A}$ is real, the top two eigenvalues (λ_1 and λ_2) and eigenvectors ($\vec{v}_1$ and $\vec{v}_2$) are either real or form a complex conjugate pair. Then, we change these eigenvectors to point along the original coordinate lines, $|a_-|, n_w$, as follows:

$$\begin{bmatrix}\vec{v}'_1\\ \vec{v}'_2\end{bmatrix} = \begin{bmatrix}v_{12} & v_{14}\\ v_{22} & v_{24}\end{bmatrix}^{-1}\begin{bmatrix}v_{12} & v_{14} & v_{11} & v_{12} & v_{13} & v_{14} & v_{15}\\ v_{22} & v_{24} & v_{21} & v_{22} & v_{23} & v_{24} & v_{25}\end{bmatrix}, \tag{13}$$

where v_{ij} are the components of the top eigenvectors of the matrix $\boldsymbol{A}$, i is the number of the top eigenvector, j indicates the component of the eigenvector. Then, the two vectors $\vec{v}'_1$ and $\vec{v}'_2$ are determined at positions of the state vector approximated by the polynomials [see Eq. (5a)] and separated by equidistant steps. The vectors are purely real and are plotted over the whole surfaces $|a_+|$, $\Delta\phi$, n_c; see Fig. 5. Subsequently, these vectors are scaled by the distance between the steps in the state vector along each direction in order to avoid an overlap and create a square grid pattern. If these vectors create an ideal square grid, then they can perfectly reconstruct the tangential vectors in Eq. (12). A small discrepancy is only found in Fig. 5(c) for small values of $|a_-|$, which can be explained by the third eigenvalue becoming comparable to the dominating pair of eigenvalues at these points; see Fig. 4. However, the two vectors $\vec{v}'_1$ and $\vec{v}'_2$ are found to approximate the tangential vectors over the whole surface, as observed in Fig. 5. Thus, the two-degrees-of-freedom picture is justified over the whole surface and is shown to precisely reconstruct $d\vec{\psi}(\tau)/d\tau$. Therefore, the system of five nonlinear differential equations can be reduced to only two differential equations after the initial transition stage. The other three dimensions are functions of n_w and $|a_-|$ and are presently approximated by polynomials. We note that the instantaneous eigenvalues and eigenvectors are not needed to reduce dimensionality of the system, but they provide an additional insight into the solution. Furthermore, the fact that the two instantaneous eigenvectors approximate the tangential vectors to the surfaces proves that the system dimensionality can be reduced to two.

Moreover, we note that although a 2D model can be used to describe the laser dynamics after the initial transition stage, there exists a parameter region in which even a 1D model is sufficient to replace the original 5D model after the initial transition stage. One may observe in Fig. 2 that for a large negative detuning $\Delta\omega_c$, the steady-state eigenvalues undergo a transition from a complex conjugate pair of eigenvalues to two purely real eigenvalues. Then, one of the eigenvalues decreases rapidly and the other one approaches zero. Therefore, for detunings $-2.05\gamma_T < \Delta\omega_c < -1.72\gamma_T$, there is a single steady-state eigenvalue that dominates and, thus, the velocity vector can be described by a single eigenvector; see Eq. (9). In this case, the laser dynamics can be described by a single differential equation after the transition stage in which the contribution from the other four eigenvalues rapidly decays. For detunings $\Delta\omega_c < -2.05\gamma_T$, the lasing mode ceases to exist [7,11,13]. Thus, as the detuning $\Delta\omega_c$ increases, the steady-state eigenvalues transition from being purely real to a complex conjugate pair and the system evolves from a 1D to a 2D system [57].

IV. ORIGIN OF THE LASER INSTABILITY

A. Detection of periodic orbits

In what follows, we use the simplified 2D model, given by Eq. (7), to explain the origin of the laser instability that

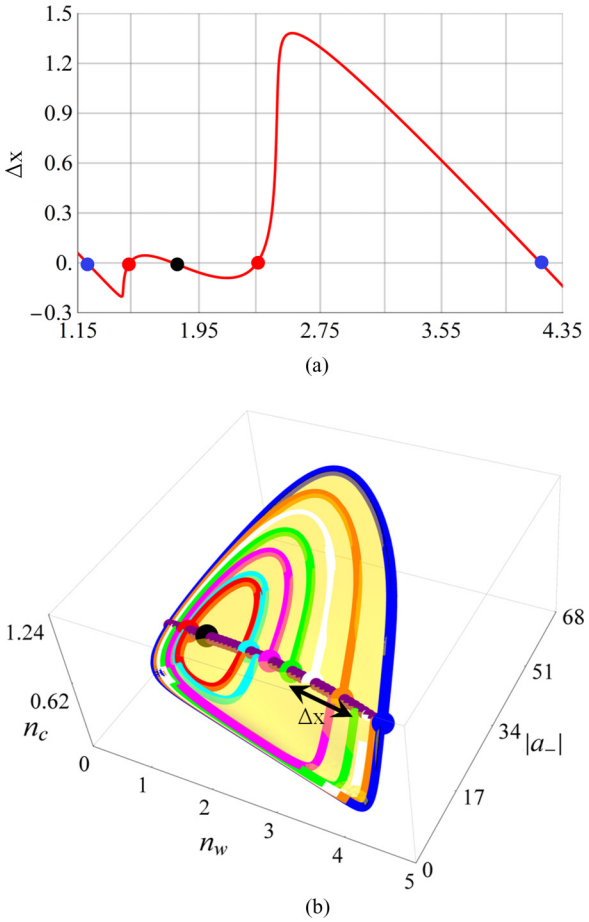

FIG. 6. (a) Numerically evaluated shift $\Delta x = n_w^{\text{initial}} - n_w^{\text{cycle}}$ in phase space after one cycle of the trajectory. The single black dot indicates the steady state; the pairs of red (gray) and blue (dark gray) dots indicate two periodic orbits. The initial value for $|a_-|$ is fixed and equal to the steady-state value, while the initial value for n_w is varied. The initial states are marked on the surface along the purple line (constant $|a_-|$) in (b). (b) A single cycle of several trajectories (marked with different colors) initiated at different initial states along the purple line on the curved surface $n_c(|a_-|, n_w)$. The initial states are marked with dots. The definition of Δx is also indicated.

may be observed even when all real parts of the steady-state eigenvalues are negative.

At first, the phase space of the Fano laser is scanned in the search for periodic orbits. We choose our initial conditions as follows: (1) $|a_-^{\text{initial}}|$ is set to the steady-state value and (2) n_w^{initial} is varied over the whole phase space along the purple line, as shown in Fig. 6(b). For each initial condition, we then compute the trajectory by solving Eq. (7) up to the point when $|a_-(T)| = |a_-^{\text{initial}}|$, where T is the time corresponding to one cycle. Some of these trajectories are shown in Fig. 6(b) in different colors. Subsequently, we evaluate the shift $\Delta x = n_w^{\text{initial}} - n_w^{\text{cycle}}$ in the state vector after the time T. If the shift between the initial state and the state after one cycle is zero, then we are at a periodic orbit or steady state. On the other hand, if it is nonzero, it means that the state is approaching or departing from the steady state or periodic orbit.

Figure 6(a) shows the numerically evaluated shift Δx in n_w after one cycle of the trajectory. It is seen that there are five crossings with zero. These crossings are marked with blue, red, and black dots. The single black dot indicates the steady state, while the pairs of blue and red dots indicate periodic orbits. The outer periodic orbit, marked with a pair of blue dots, has been observed before and is known to be stable for a pair of complex conjugate steady-state eigenvalues with a positive real part [11]. Here, it is seen that for a strong enough perturbation of the initial conditions from the steady-state value, the state can still reach the outer periodic orbit despite all the steady-state eigenvalues having a negative real part and thus the steady state being stable and attracting the state. Furthermore, we find an additional periodic orbit marked with a pair of red dots in Fig. 6(a). This found periodic orbit separates the steady state and the outer periodic orbit.

B. Stability of the orbits

We now prove the stability of this found orbit using the simplified 2D model. This is done by calculating the Floquet multipliers λ_f, which tell us how the solution behaves in the vicinity of the periodic orbit, i.e., whether it diverges or converges from or towards the orbit [58,59]. In order to compute the Floquet multipliers, we first obtain the fundamental solution matrix $\mathbf{\Phi}(\tau)$, which can be determined using $d\mathbf{\Phi}(\tau)/d\tau = \boldsymbol{A}(\tau)\mathbf{\Phi}(\tau)$ and satisfies $d\vec{\psi}/d\tau = \mathbf{\Phi}(\tau)d\vec{\psi}/d\tau|_{\tau=0}$ with $\mathbf{\Phi}(0) = \boldsymbol{I}$. The Floquet multipliers are the eigenvalues of $\mathbf{\Phi}(\tau)$ evaluated at $\tau = T$, where T is the period of the orbit.

If the Floquet multipliers are within the unit circle in the complex plane, the orbit is stable, otherwise it is unstable. The Floquet multipliers for the outer periodic orbit are $\lambda_{f1} = 0.04$ and $\lambda_{f2} = 1$, confirming its stability. On the other hand, the Floquet multipliers of the found orbit are $\lambda_{f1} = 2.31$ and $\lambda_{f2} = 1$, proving that this orbit is unstable. We note that for a periodic orbit, there is always one of the Floquet multipliers for which $\lambda_f = 1$ and the corresponding eigenvector is tangential to the periodic orbit. This neutral stability accounts for the possibility of drift along the periodic orbit [58].

Furthermore, we study the stability of the found orbit with variation of the detuning, $\Delta\omega_c$. It is observed that the Floquet multiplier crosses the unit circle along the real axis in the complex plane. This indicates an exchange of instability [50]. Indeed, as $\Delta\omega_c$ decreases from $\Delta\omega_c = 0.52\gamma_T$ (see Fig. 2), the found unstable periodic orbit increases in size. Eventually, it collapses with the stable periodic orbit. Both orbits disappear due to a fold bifurcation [18] and only the stable (time-independent) steady state remains present in the phase space. On the other hand, when $\Delta\omega_c$ increases, the unstable orbit decreases in size. Eventually, it collapses with the stable steady state, resulting in the steady state becoming unstable. This happens in the vicinity of $\Delta\omega_c = 1.52\gamma_T$, which is the critical bifurcation point and, as $\Delta\omega_c$ is increased further, the real part of the steady-state eigenvalues becomes positive. Since the cycle is present before the bifurcation point, i.e., before the real parts of the steady-state eigenvalues become positive, the bifurcation at this point is called a subcritical Hopf bifurcation.

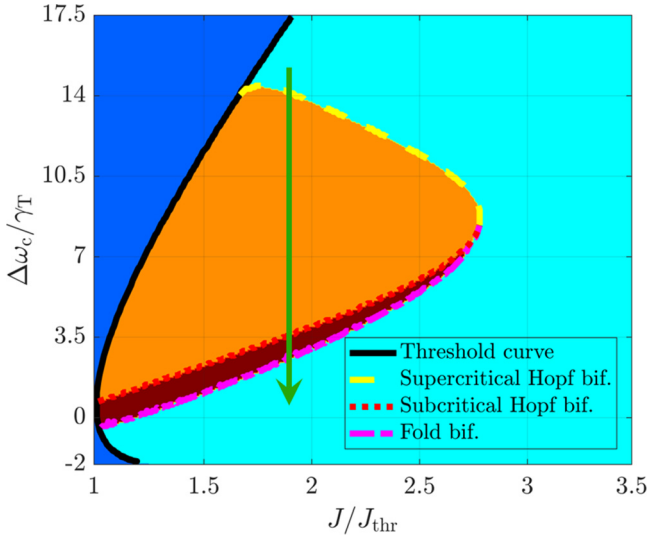

FIG. 7. Phase diagram of the Fano laser as a function of pump current J/J_{thr} and cavity detuning $\Delta\omega_c/\gamma_T$. Blue indicates solutions below threshold (the dark gray area on the left of the black solid curve); cyan (light gray) marks a stable continuous-wave solution. Orange (gray) indicates the presence of a stable limit cycle and an unstable steady state, while dark red (the dark gray area between the dotted and the dash-dotted lines) indicates two orbits being present, stable and unstable, as well as a stable steady state. The laser threshold curve is shown in black. The dashed yellow line and dotted red line mark the supercritical and subcritical Hopf bifurcations, respectively. The dash-dotted magenta line indicates a fold bifurcation.

Both bifurcations are marked in the phase diagram in Fig. 7. It shows that as $\Delta\omega_c$ is decreased from large values along the dark green arrow, at first the system undergoes a supercritical Hopf bifurcation at the dashed yellow line. There, the real part of the steady-state eigenvalues crosses zero and becomes positive, resulting in the steady-state point becoming unstable and a stable limit cycle being present after the bifurcation point. As we decrease $\Delta\omega_c$ further, the system undergoes a subcritical Hopf bifurcation at the dotted red line. Here, the steady-state point becomes stable again, while the stable periodic orbit coexists with an unstable periodic orbit. Eventually, as $\Delta\omega_c$ is further decreased, the unstable periodic orbit collides with the stable one, and both orbits disappear through a fold bifurcation, leaving the stable steady-state point as the only solution [18,50]. Analogous behavior is observed for lower pump currents including $J = 1.2J_{\text{thr}}$; however, in this case, the laser is below threshold for large detuning $\Delta\omega_c$.

The occurrence of both Hopf bifurcations, i.e., supercritical and subcritical, is a signature of a Bautin bifurcation, also known as the generalized Hopf bifurcation [17,18]. A Bautin bifurcation is characterized by the presence of two orbits and an equilibrium point (steady state) in phase space. We note that a Bautin bifurcation cannot be detected by merely monitoring the eigenvalues [17,18]. Upon the external parameter variation $\Delta\omega_c$, an inner orbit may collide with an outer orbit and annihilate or exchange stability with an equilibrium point, as has been observed. We note that since each $\Delta\omega_c$ results in different solutions (ω_s, N_s) of the oscillation condition in Eq. (1), we adjust the polynomial approximation of the surface in each case.

The stability of the orbits can also be assessed based on Fig. 6(a). It is seen that if the model is slightly perturbed from the orbit marked with the red dots, the perturbation will increase after one cycle. Thus, the state is always repelled away from the orbit, confirming that the found orbit is unstable.

V. CONCLUSION

We demonstrate that after a fast initial transient, the dynamics of the recently realized Fano laser [10] are confined to a 2D center manifold. The dimension of the center manifold follows the number of steady-state eigenvalues, the real parts of which cross zero. We show that there are two steady-state eigenvalues with real parts crossing zero, while the remaining three eigenvalues have negative real parts forming a stable manifold. The dynamics is attracting along the corresponding three directions and quickly tends to the curved surface, i.e., the center manifold, during the initial transition stage. Afterwards, the state vector is confined to the curved surface and can be solely described by two degrees of freedom. The surface geometry of the phase space can be approximated by the two eigenvectors of the linear stability matrix corresponding to the eigenvalues with the largest real parts. As the pulse develops, the instantaneous eigenvalues transition from a pair of purely real eigenvalues to a complex conjugate pair at the first exceptional point. The main part of the repeating pulse is bounded by two exceptional points with a positive and negative real part of the eigenvalue at the beginning and end of the pulse, respectively. Moreover, the trajectory encounters four exceptional points during one period, ensuring that both the eigenvalues and eigenvectors are periodic in τ. Furthermore, we show that the 5D model used to describe the laser dynamics, after the initial transition stage, can be reduced to only 1D in part of the parameter space and evolves into a 2D model beyond the exceptional point of the steady-state eigenvalues as the detuning $\Delta\omega_c$ increases. Moreover, we have used the simplified 2D model to associate the unknown source of laser instability with the found unstable periodic orbit, which arises due to a generalized Hopf (Bautin) bifurcation. These findings allow one to better understand the laser dynamics and may lead to the design of new functionalities in nanolasers used for on-chip communications and sampling.

ACKNOWLEDGMENTS

The authors would like to thank T. S. Rasmussen for helpful discussions on the implementation of the dynamic model. This work was supported by the Villum Fonden via the Centre of Excellence NATEC (Grant No. 8692) and the Research Grants Council of Hong Kong through Project No. C6013-18G.

[1] D. A. B. Miller, Device requirements for optical interconnects to silicon chips, Proc. IEEE **97**, 1166 (2009).

[2] Y. Akahane, T. Asano, B.-S. Song, and S. Noda, High-Q photonic nanocavity in a two-dimensional photonic crystal, Nature (London) **425**, 944 (2003).

[3] N.-V.-Q. Tran, S. Combrié, and A. De Rossi, Directive emission from high-Q photonic crystal cavities through band folding, Phys. Rev. B **79**, 041101(R) (2009).

[4] S. Matsuo, T. Sato, K. Takeda, A. Shinya, K. Nozaki, H. Taniyama, M. Notomi, K. Hasebe, and T. Kakitsuka, Ultralow operating energy electrically driven photonic crystal lasers, IEEE J. Sel. Top. Quantum **19**, 4900311 (2013).

[5] H. Jang, I. Karnadi, P. Pramudita, J.-H. Song, K. S. Kim, and Y.-H. Lee, Sub-microWatt threshold nanoisland lasers, Nat. Commun. **6**, 8276 (2015).

[6] P. Hamel, S. Haddadi, F. Raineri, P. Monnier, G. Beaudoin, I. Sagnes, A. Levenson, and A. M. Yacomotti, Spontaneous mirror-symmetry breaking in coupled photonic-crystal nanolasers, Nat. Photon. **9**, 311 (2015).

[7] J. Mork, Y. Chen, and M. Heuck, Photonic Crystal Fano Laser: Terahertz Modulation and Ultrashort Pulse Generation, Phys. Rev. Lett. **113**, 163901 (2014).

[8] U. Fano, Effects of Configuration Interaction on Intensities and Phase Shifts, Phys. Rev. **124**, 1866 (1961).

[9] M. F. Limonov, M. V. Rybin, A. N. Poddubny, and Y. S. Kivshar, Fano resonances in photonics, Nat. Photon. **11**, 543 (2017).

[10] Y. Yu, W. Xue, E. Semenova, K. Yvind, and J. Mørk, Demonstration of a self-pulsing photonic crystal Fano laser, Nat. Photon. **11**, 81 (2017).

[11] T. S. Rasmussen, Y. Yu, and J. Mørk, Theory of self-pulsing in photonic crystal fano lasers, Laser Photon. Rev. **11**, 1700089 (2017).

[12] T. S. Rasmussen, Y. Yu, and J. Mørk, Modes, stability, and small-signal response of photonic crystal Fano lasers, Opt. Express **26**, 16365 (2018).

[13] J. Mørk, B. Tromborg, and J. Mark, Chaos in semiconductor lasers with optical feedback: theory and experiment, IEEE J. Quantum Electron. **28**, 93 (1992).

[14] B. Krauskopf, Bifurcation analysis of laser systems, in *Nonlinear Laser Dynamics: Concepts, Mathematics, Physics, and Applications International Spring School*, edited by B. Krauskopf and D. Lenstra, AIP Conf. Proc. No. 548 (AIP, The Netherlands, 2000), pp. 1–30.

[15] S. Wieczorek, B. Krauskopf, T. B. Simpson, and D. Lenstra, The dynamical complexity of optically injected semiconductor lasers, Phys. Rep. **416**, 1 (2005).

[16] H. Erzgräber, B. Krauskopf, and D. Lenstra, Bifurcation analysis of a semiconductor laser with filtered optical feedback, SIAM J. Appl. Dynam. Sys. **6**, 1 (2007).

[17] W. Govaerts, Y. A. Kuznetsov, and B. Sijnave, Numerical methods for the generalized hopf bifurcation, SIAM J. Numer. Anal. **38**, 329 (2000).

[18] Y. Kuznetsov, *Elements of Applied Bifurcation Theory*, 3rd ed. (Springer, New York, 2004).

[19] S. Fan, W. Suh, and J. D. Joannopoulos, Temporal coupled-mode theory for the Fano resonance in optical resonators, J. Opt. Soc. Am. A **20**, 569 (2003).

[20] W. Suh, Z. Wang, and S. Fan, Temporal coupled-mode theory and the presence of non-orthogonal modes in lossless multimode cavities, IEEE J. Quantum Electron. **40**, 1511 (2004).

[21] P. T. Kristensen, J. R. de Lasson, M. Heuck, N. Gregersen, and J. Mørk, On the theory of coupled modes in optical cavity-waveguide structures, J. Lightwave Technol. **35**, 4247 (2017).

[22] B. Tromborg, H. Olesen, X. Pan, and S. Saito, Transmission line description of optical feedback and injection locking for Fabry-Perot and DFB lasers, IEEE J. Quantum Electron. **23**, 1875 (1987).

[23] P. McCord Morse, H. Feshbach, and G. P. Harnwell, *Methods of Theoretical Physics, Part I* (McGraw-Hill, Boston, 1953).

[24] S. Ibáñez and J. G. Muga, Adiabaticity condition for non-hermitian Hamiltonians, Phys. Rev. A **89**, 033403 (2014).

[25] G. B. Arfken and H. J. Weber, *Mathematical Methods for Physicists*, 6th ed. (Academic, Boston, 2005).

[26] C. Dembowski, H.-D. Gräf, H. L. Harney, A. Heine, W. D. Heiss, H. Rehfeld, and A. Richter, Experimental Observation of the Topological Structure of Exceptional Points, Phys. Rev. Lett. **86**, 787 (2001).

[27] W. D. Heiss, Exceptional points – their universal occurrence and their physical significance, Czech. J. Phys. **54**, 1091 (2004).

[28] M. V. Berry, Physics of nonhermitian degeneracies, Czech. J. Phys. **54**, 1039 (2004).

[29] W. D. Heiss, The physics of exceptional points, J. Phys. A: Math. Theor. **45**, 444016 (2012).

[30] M. Liertzer, L. Ge, A. Cerjan, A. D. Stone, H. E. Türeci, and S. Rotter, Pump-Induced Exceptional Points in Lasers, Phys. Rev. Lett. **108**, 173901 (2012).

[31] C. M. Bender, M. V. Berry, and A. Mandilara, Generalized PT symmetry and real spectra, J. Phys. A: Math. Gen. **35**, L467 (2002).

[32] C. E. Rüter, K. G. Makris, R. El-Ganainy, D. N. Christodoulides, Mordechai Segev, and Detlef Kip, Observation of parity-time symmetry in optics, Nat. Phys. **6**, 192 (2010).

[33] L. Feng, R. El-Ganainy, and L. Ge, Non-Hermitian photonics based on parity-time symmetry, Nat. Photon. **11**, 752 (2017).

[34] R. El-Ganainy, K. G. Makris, M. Khajavikhan, Z. H. Musslimani, S. Rotter, and D. N. Christodoulides, Non-Hermitian physics and PT symmetry, Nat. Phys. **14**, 11 (2018).

[35] S. Klaiman, U. Günther, and N. Moiseyev, Visualization of Branch Points in $\mathcal{PT}$-Symmetric Waveguides, Phys. Rev. Lett. **101**, 080402 (2008).

[36] M. V. Berry, Mode degeneracies and the Petermann excess-noise factor for unstable lasers, J. Mod. Opt. **50**, 63 (2003).

[37] K.-H. Kim, M.-S. Hwang, H.-R. Kim, J.-H. Choi, Y.-S. No, and H.-G. Park, Direct observation of exceptional points in coupled photonic-crystal lasers with asymmetric optical gains, Nat. Commun. **7**, 13893 (2016).

[38] R. Lefebvre, O. Atabek, M. Šindelka, and N. Moiseyev, Resonance Coalescence in Molecular Photodissociation, Phys. Rev. Lett. **103**, 123003 (2009).

[39] T. Stehmann, W. D. Heiss, and F. G. Scholtz, Observation of exceptional points in electronic circuits, J. Phys. A: Math. Gen. **37**, 7813 (2004).

[40] H. Xu, D. Mason, L. Jiang, and J. G. E. Harris, Topological energy transfer in an optomechanical system with exceptional points, Nature (London) **537**, 80 (2016).

[41] W. D. Heiss, Repulsion of resonance states and exceptional points, Phys. Rev. E **61**, 929 (2000).

[42] I. Rotter, A non-Hermitian Hamilton operator and the physics of open quantum systems, J. Phys. A: Math. Theor. **42**, 153001 (2009).

[43] Y. D. Chong, L. Ge, and A. D. Stone, $\mathcal{PT}$-Symmetry Breaking and Laser-Absorber Modes in Optical Scattering Systems, [Phys. Rev. Lett. 106, 093902 (2011)], Phys. Rev. Lett. **108**, 269902 (2012).

[44] G. W. Hanson, A. B. Yakovlev, M. A. K. Othman, and F. Capolino, Exceptional points of degeneracy and branch points for coupled transmission lines-linear-algebra and bifurcation theory perspectives, IEEE Trans. Antennas Propag. **67**, 1025 (2019).

[45] U. Bandelow, H. J. Wunsche, and H. Wenzel, Theory of self-pulsations in two-section DFB lasers, IEEE Photonics Technol. Lett. **5**, 1176 (1993).

[46] H. Wenzel, U. Bandelow, H.-J. Wunsche, and J. Rehberg, Mechanisms of fast self pulsations in two-section DFB lasers, IEEE J. Quantum Electron. **32**, 69 (1996).

[47] L. Feng, Z. J. Wong, R.-M. Ma, Y. Wang, and X. Zhang, Single-mode laser by parity-time symmetry breaking, Science **346**, 972 (2014).

[48] H. Hodaei, M.-A. Miri, M. Heinrich, D. N. Christodoulides, and M. Khajavikhan, Parity-time-symmetric microring lasers, Science **346**, 975 (2014).

[49] J. Guckenheimer and P. Holmes, *Nonlinear Oscillations, Dynamical Systems, and Bifurcations of Vector Fields* (Springer-Verlag, New York, 1983).

[50] R. Seydel, *Practical Bifurcation and Stability Analysis*, Number 5 in Interdisciplinary Applied Mathematics, 3rd ed. (Springer, New York, 2010).

[51] U. Günther, I. Rotter, and B. F. Samsonov, Projective Hilbert space structures at exceptional points, J. Phys. A: Math. Theor. **40**, 8815 (2007).

[52] F. Keck, H. J. Korsch, and S. Mossmann, Unfolding a diabolic point: A generalized crossing scenario, J. Phys. A: Math. Gen. **36**, 2125 (2003).

[53] M. Müller and I. Rotter, Exceptional points in open quantum systems, J. Phys. A: Math. Theor. **41**, 244018 (2008).

[54] H. Menke, M. Klett, H. Cartarius, J. Main, and G. Wunner, State flip at exceptional points in atomic spectra, Phys. Rev. A **93**, 013401 (2016).

[55] W. D. Heiss, M. Müller, and I. Rotter, Collectivity, phase transitions, and exceptional points in open quantum systems, Phys. Rev. E **58**, 2894 (1998).

[56] W. D. Heiss, Phases of wave functions and level repulsion, Eur. Phys. J. D **7**, 1 (1999).

[57] P. M. Kamiński, Active nanophotonic antenna arrays for effective light-matter interactions, Ph.D. thesis, Technical University of Denmark, 2019.

[58] P. Glendinning, *Stability, Instability and Chaos: An Introduction to the Theory of Nonlinear Differential Equations*, 1st ed. (Cambridge University Press, Cambridge, 1994).

[59] G. Iooss and D. D. Joseph, *Elementary Stability and Bifurcation Theory*, 2nd ed. (Springer, New York, 1997).